

Emerging magnetism and electronic phase separation at titanate interfaces

N. Pavlenko^{1,2}, T. Kopp¹, and J. Mannhart²

¹ *EKM and Institut für Physik, Universität Augsburg, 86135 Augsburg, Germany*

² *Max Planck Institute for Solid State Research, Heisenbergstr.1, Stuttgart, Germany*

(Dated: March 3, 2022)

The emergence of magnetism in otherwise nonmagnetic compounds and its underlying mechanisms have become the subject of intense research. Here we demonstrate that the nonmagnetic oxygen vacancies are responsible for an unconventional magnetic state common for titanate interfaces and surfaces. Using an effective multiorbital modelling, we find that the presence of localized vacancies leads to an interplay of ferromagnetic order in the itinerant t_{2g} band and complex magnetic oscillations in the orbitally-reconstructed e_g -band, which can be tuned by gate fields at oxide interfaces. The magnetic phase diagram includes highly fragmented regions of stable and phase-separated magnetic states forming beyond nonzero critical defect concentrations.

PACS numbers: 74.81.-g, 74.78.-w, 73.20.-r, 73.20.Mf

The possibility to induce a magnetic state at interfaces and surfaces of otherwise nonmagnetic titanates by introducing defects like oxygen vacancies is an open question that is in the focus of present research [1–16]. More recent studies of this problem are related to the interfaces between the bulk insulators LaAlO_3 (LAO) and SrTiO_3 (STO) [1, 17–21], for which low-temperature torque magnetometry, scanning SQUID and magnetoresistance studies [3–6] provide evidence for an inhomogeneous electronic state with coexisting superconducting (diamagnetic), ferromagnetic/superparamagnetic and paramagnetic mesoscale regions. Unlike carrier-induced ferromagnetism in diluted magnetic semiconductors, the oxygen defects are intrinsically nonmagnetic which implies that the build-up of magnetism should involve a magnetization of defects at an initial stage.

New insight into the local electronic state of oxygen-reduced titanate layers has been recently gained from DFT studies [22–24] that identified stable local magnetic moments of spin-polarized Ti $3d$ -states in the proximity of oxygen defects, which induce quasi two-dimensional (2d) ferromagnetic order at the LAO/STO interface. Although the DFT-studies associate the interface magnetism to the local nonstoichiometries, they frequently impose artificially ordered states by inevitably restricting the analysis to selected supercell configurations. Such DFT studies are usually limited to the consideration of local electron states with high defect concentration [25, 26].

As a consequence, the build-up of the spin-polarization and inhomogeneous state at titanate interfaces for different levels of defect concentration and its relation to random defects like oxygen vacancies remains unresolved. To understand the mechanism of the spin-polarization in the presence of a finite density of oxygen defects and for different mobile carrier densities, we consider a microscopic modelling of the 2d electron liquid at titanate interfaces in an external electrostatic field applied across the gate STO-layer.

The challenge that we face is to explore if a multiband model with randomly occupied defect band allows for the formation of the robust magnetic state at the micro- and nanoscales—even though the defects are non-magnetic in the dilute limit. In particular, is there a finite critical density of defects where magnetism sets in? DFT studies are not appropriate to assess whether such a critical density exists.

For clarity we analyze a two-orbital model on an N -site square lattice with random occupation of the second orbital. The Hamiltonian below is to be taken as an effective Hamiltonian for the 2d electron system at the LAO/STO interface with the lowest Ti t_{2g} band partially occupied, viz. the itinerant Ti $3d_{xy}$ band (label $\alpha = 1$), and with an oxygen-defect relevant Ti e_g band (label $\alpha = 2$). In contrast to stoichiometric SrTiO_3 with empty high-energy e_g bands, the $3d$ orbital reconstruction due to the oxygen vacancies [23] modifies the local covalent bonding and shifts down the local e_g -level of the Ti in the proximity of vacancy, which leads to a random electronic occupation of the band $\alpha = 2$ by vacancy-released $3d$ -electrons (Fig. 1):

$$H_{OR} = (\varepsilon_d - \mu) \sum_{\substack{i=1 \\ \sigma=\uparrow,\downarrow}}^N n_{i,1,\sigma} + \sum_{\substack{i=1 \\ \sigma}}^N (\varepsilon_d - \mu + \phi_{i\sigma}) n_{i,2,\sigma} \quad (1)$$

Here the electron number operators $n_{i,\alpha,\sigma} = c_{i,\alpha,\sigma}^\dagger c_{i,\alpha,\sigma}$, where $c_{i,\alpha,\sigma}^\dagger$ are electron creation operators, σ is the electron spin index, μ is the chemical potential, and ε_d is the $3d_{xy}$ reference energy level of Ti. The field $\phi_{i\sigma} = \sum_{l=1,4} (x_{il} \Delta_o - (1 - x_{il}) \Delta_v)$ depends on the local values of random variables $\{x_{il}\} = 0, 1$ which correspond to the presence or absence of oxygen atoms (i, l) in the nearest oxygen configuration around the i -th Ti atom. In the stoichiometric heterostructure, the octahedral field splits the two considered $3d$ levels by a gap $4\Delta_o$ which is obtained by setting all local variables $x_{il} = 1$ in the field $\phi_{i\sigma}$. In contrast, in the system with oxygen defects, recent DFT studies of LAO-STO [23] reveal an electronic

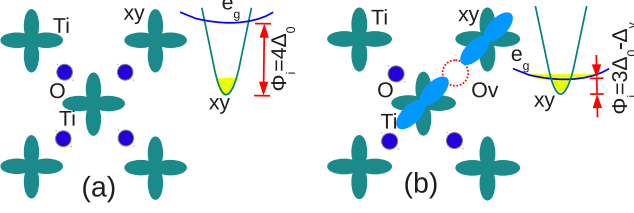


FIG. 1: Scheme of vacancy-induced orbital reconstruction in the STO interface layer with a strong negative shift and partial electron occupation of the e_g orbital (b) of a Ti_2O_4 -plaquette. The initial stoichiometric configuration with electron-occupied $3d_{xy}$ levels of Ti is shown in (a). The occupied electron states are yellow-colored.

occupation of the Ti e_g state due to oxygen vacancies in the positions (i, l) . The resulting negative shift $-\Delta_v$ of the e_g energy level is described by setting the value of x_{il} in (1) to zero. From the DFT studies, we estimate the energies $\Delta_o \approx 0.7\text{eV}$ and $\Delta_v \approx 1.2\text{--}2.4\text{eV}$. Additional terms describe the local Coulomb repulsion and kinetic electron inter- and intra-orbital exchange (cf. [28])

$$H_C = U \sum_{\alpha, i} n_{i, \alpha, \uparrow} n_{i, \alpha, \downarrow} + U' \sum_i n_{i, 1} n_{i, 2} \quad (2)$$

$$+ J_H \sum_i (b_{i, \uparrow} b_{i, \downarrow} + h.c.) - 2J_H \sum_i \vec{S}_{i1} \vec{S}_{i2}$$

$$- \sum_{\alpha; \sigma; \langle i, j \rangle} t_\alpha (c_{i, \alpha, \sigma}^\dagger c_{j, \alpha, \sigma} + h.c.)$$

Here $b_{i\sigma} = c_{i, 1, \sigma}^\dagger c_{i, 2, \sigma}$ is an interband operator; $U = 2\text{eV}$ is the Coulomb repulsion energy for $3d$ Ti electrons [29], J_H is the Hund coupling energy, and $U' = U - 2J_H$. The three-component band spin operator $S_{i\alpha}$ is defined as $S_{i\alpha} = \left\{ c_{i, \alpha, \uparrow}^\dagger c_{i, \alpha, \downarrow}, c_{i, \alpha, \downarrow}^\dagger c_{i, \alpha, \uparrow}, \frac{1}{2}(n_{i, \alpha, \uparrow} - n_{i, \alpha, \downarrow}) \right\}$, and the electron orbital operators as $n_{i, \alpha} = \sum_\sigma n_{i, \alpha, \sigma}$. From the DFT band structure calculations, we obtain the effective electron transfer energy $t_1 = 0.28\text{eV}$ of the lowest $3d_{xy}$ Ti band. The strong-localization character of the orbitally-reconstructed e_g band results from a much smaller value of t_2 , viz. $t_2/t_1 = 0.05$. In the following analysis, the energy parameters are scaled by t_1 .

The interaction of electron charges with polar electrostatic fields shifts the electron energies $H_{FE} = -E_g \sum_{i, \alpha} n_{i, \alpha}$ by the value $E_g = (de)V_g$, where V_g is the external gate field [40], d is the thickness of the gate layer and e is the electron charge [30, 31].

To analyze the thermodynamic state of the model (1)–(2) in a weak and moderate Coulomb-coupling regime, we employ a generalized molecular-field approach, which contains, besides the mean-field type decoupling of the correlations terms in (2) and thermodynamical averaging, an additional configuration averaging with respect to the local random configurational fields ϕ_i . We assume independence of each local configuration in the i -th unit

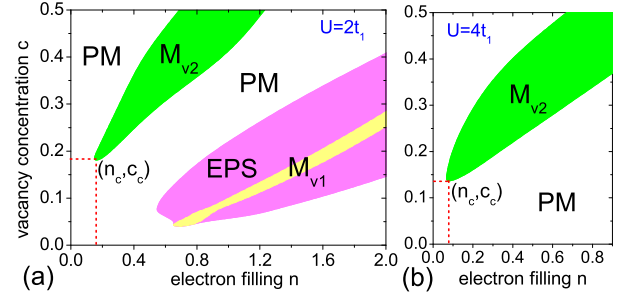


FIG. 2: Typical diagram of magnetic phases predicted for LAO-STO interfaces. The phase diagram (a) is obtained for $J_H/t_1 = 1.8$, $k_B T/t_1 = 0.03$, $\Delta_o/t_1 = 2.0$, $\Delta_v/t_1 = 6.0$, $U/t_1 = 2$. The red color marks the regimes with electronic phase separation (EPS) of paramagnetic and magnetic state M_{v1} . (b) Detailed view of the phase M_{v2} for $U/t_1 = 4$.

cell on the local configurations of the surrounding cells, in the spirit of the virtual-crystal approach (VCA) [32]. The resulting configurationally averaged grand canonical thermodynamic potential is given by

$$\frac{\Omega}{N} = -\xi_0 - k_B T (1-c)^4 \sum_{\substack{j=0 \\ \alpha=1, 2; \sigma}}^4 \sum_{\vec{k}} p_j \ln(1 + e^{-\lambda_{\alpha\sigma}^j(\vec{k})/k_B T})$$

where the configurational weight $p_j = p_j^0 \left(\frac{c}{1-c} \right)^j$ depends on the average concentration (probability) of the oxygen defects $c = 1 - x$ determined through $x = \frac{1}{4N} \sum_{i, l} \langle x_{il} \rangle$; the vector $\{p_j^0\} = \{1, 4, 6, 4, 1\}$ contains the statistical contributions of random vacancy configurations of each TiO_4 -plaquette with $j = 0, \dots, 4$ vacancies near the Ti-atom. The orbital- and spin-projected band energies are given by $\lambda_{\alpha\sigma}^j(\vec{k}) = \Pi_\sigma(\vec{k}) + \phi_\sigma^j/2 - (-1)^\alpha s_{j\sigma}(\vec{k})/2$, where $\Pi_\sigma(\vec{k}) = \varepsilon_d - \varepsilon_g - \mu + \frac{3}{2}(\frac{U}{2} - J_H)n - \sigma \frac{U+J_H}{4}(m + t\eta_{\vec{k}})$ with the magnetization $m = \sum_\alpha m_\alpha$ and the kinetic parameter $t = \sum_\alpha t_\alpha$ with $\eta_{\vec{k}} = \cos k_x + \cos k_y$. The interband splitting $s_{j\sigma}(\vec{k}) = \sqrt{(\Delta\varepsilon_\sigma(\vec{k}) - \phi_\sigma^j)^2 + 4J_H^2 |\langle b_\sigma \rangle|^2}$ depends on the interorbital gap $\Delta\varepsilon_\sigma(\vec{k}) = (-\frac{U}{2} + 3J_H)\delta - \sigma \frac{U-J_H}{2}(m_1 - m_2) + 2(t_1 - t_2)\eta_{\vec{k}}$, the charge order parameter $\delta = \langle n_1 \rangle - \langle n_2 \rangle$, and orbital magnetization $m_\alpha = \langle n_{\alpha\uparrow} \rangle - \langle n_{\alpha\downarrow} \rangle$. For each unit cell, the local field vector $\{\phi_\sigma^j\} = \phi_{i\sigma}(\{x_{il}\}) = \{4\Delta_o; 3\Delta_o - \Delta_v; 2(\Delta_o - \Delta_v); \Delta_o - 3\Delta_v; 4\Delta_v\}$ represents possible values of $\phi_{i\sigma}$ in the local random vacancy-configuration environment with j vacancies near each Ti atom. The quadratic term $\xi_0 = \frac{U}{4}(\frac{1}{2}(n^2 + \delta^2) - (m_1^2 + m_2^2)) + \frac{1}{4}(U - 3J_H)(n^2 - \delta^2) + J_H(\langle b_\uparrow^\dagger \rangle \langle b_\downarrow \rangle + h.c.)$ contains the thermodynamically and configurationally averaged order parameters which can be self-consistently determined from the corresponding extremum conditions for Ω .

To explore the magnetic states, we investigate interface thermodynamic phases by minimization of Ω with respect to m_α , $\langle b_\sigma \rangle$ and δ . Fig. 2 shows a characteristic

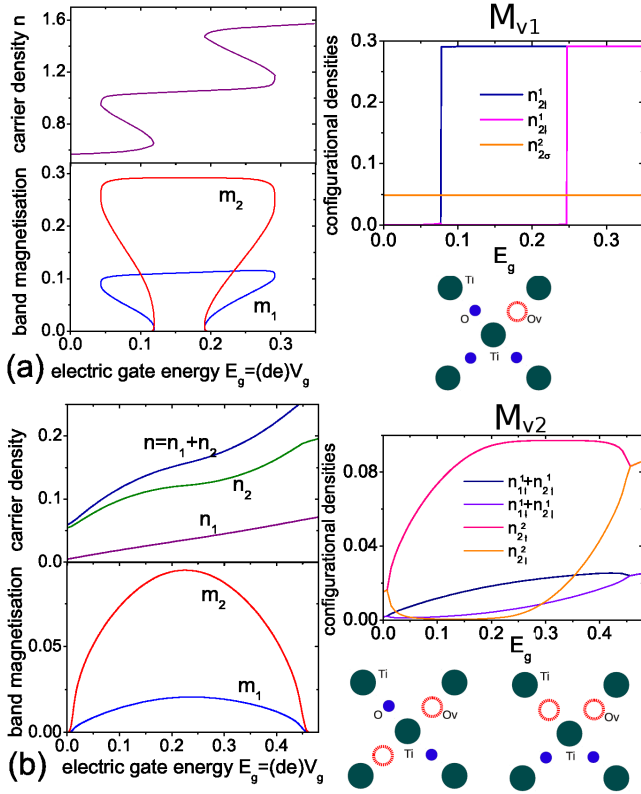


FIG. 3: Electron carrier density and band magnetisation versus electric-gate-induced energy E_g (a) in the phase M_{v1} , with $\mu/t_1 = -1.4$, $c = 0.1$, $U = 2t_1$ and (b) in the phase M_{v2} , with $\mu/t_1 = -3.9$, $c = 0.15$, $U = 4t_1$. Here $J_H = 1.8t_1$, $k_B T/t_1 = 0.03t_1$, $\Delta_o = 2t_1$. The plots at the rhs show the variation of the configurationally resolved contributions to the band occupancies. The superindices refer to the number of O-vacancies next to the central Ti-atom in the displayed clusters.

phase diagram (n, c) . For nonzero defect concentration c , we find, besides the trivial paramagnetic state corresponding to $m_\alpha = 0$, two different magnetic phases indicated by M_{vj} ($j = v1, v2$), where the indices v and $j = 1, 2$ signify the physical nature of magnetic ordering induced by vacancies. The magnetic phases M_{v1} and M_{v2} are characterized by non-zero polarization in both, itinerant ($\alpha = 1$)- and localized ($\alpha = 2$)-bands. The magnetic regions are highly fragmented. The phase M_{v1} is bounded by the red-colored regions of electronic phase separation characterized by the separation of the electron liquid into lower-concentration paramagnetic and higher-concentration spin-polarized states.

The contributions of different local vacancy configurations to the microscopic parameters like band filling $\langle n_{\sigma\alpha} \rangle$ and magnetization m_α are related to the random field vector $\{\phi_\sigma^j\}$ and depend on the reconstruction parameter Δ_v . Small values of $\Delta_v \leq 3\Delta_o = 6t_1$ correspond to a small and positive one-vacancy local field component $\phi_\sigma^1 = 3\Delta_o - \Delta_v = 2t_1$ and result in negligible contri-

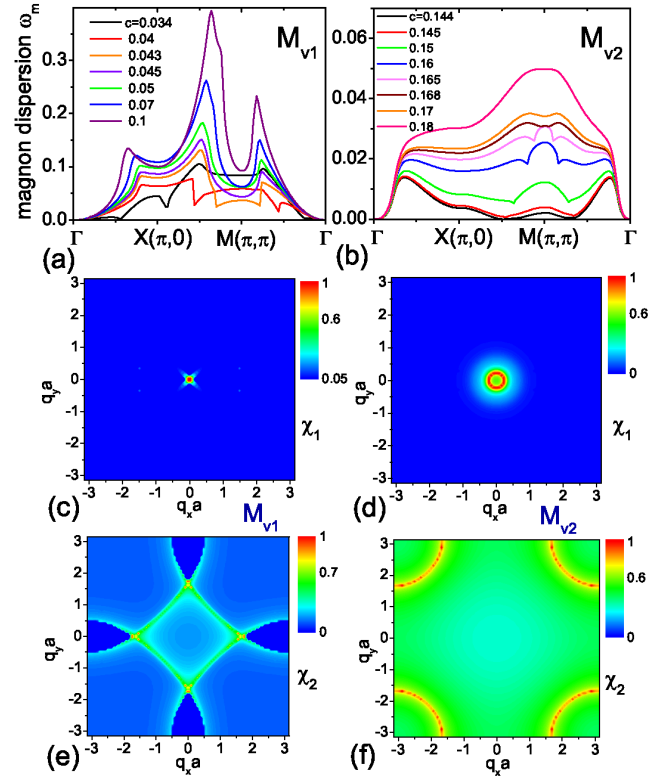


FIG. 4: Magnon dispersion energies for different defect concentration c (a) in the M_{v1} state with $U = 2t_1$, $\Delta_v = 6t_1$ and (b) in the M_{v2} state with $U = 4t_1$, $\Delta_v = 4t_1$. Here $J_H/t_1 = 1.8$, $k_B T/t_1 = 0.03$, $\Delta_o/t_1 = 2.0$, $\Delta_v/t_1 = 4.0$. The contours (c), (d), and (e), (f) display the imaginary part of the Lindhard functions $\chi_\alpha^{+-}(\vec{q}, 0)$ (scaled by their maximal values) for $\alpha = 1$ and $\alpha = 2$, respectively: left, in the magnetic state M_{v1} , and right, in M_{v2} .

butions of one-vacancy-configurations to the occupancy $\langle n_2 \rangle$ of the localized band ($\alpha = 2$), which becomes more significant only for large $n > 1$. In this case, the pronounced negative shift of the localized ($\alpha = 2$)-band level comes from the two-vacancy configurations represented by the local field component $\phi_\sigma^2 = 2(\Delta_o - \Delta_v)$, which is close to the stripe- and cluster-type configurations with two vacancies near each Ti-atom. Furthermore, the less clusterized one-vacancy (Ti-O_v-Ti dimer) configurations become important as the reconstruction parameter is increased to $\Delta_v \geq 6t_1$. This increase leads to zero or negative value of the field ϕ_σ^1 and in this way sets the energies of the itinerant ($\alpha = 1$)- and localized ($\alpha = 2$)-bands to the same level. As a result, the parameter Δ_v determines the configurational character of the electronic properties and describes the clusterization level of the oxygen vacancies which can be controlled by vacancy diffusion in external electric fields.

We address now the properties of the magnetic states M_{v1} and M_{v2} . Both M_{v1} and M_{v2} appear at finite critical defect concentrations and are induced by oxygen defects.

A remarkable feature of the phase diagrams in Fig. 2 is the existence of the critical (cusp) point (c_c, n_c) terminating the vacancy-induced magnetic state M_{v2} . The cusp implies the existence of a lowest nonzero vacancy concentration $c_c \approx 0.1$ that is necessary for the stabilization of the state M_{v2} . The decrease of the Coulomb repulsion U from $U/t_1 = 4$ (Fig. 2(b)) to $U/t_1 = 2$ (Fig. 2(a)) increases the critical vacancy concentrations c_c from 0.13 to ~ 0.2 . The origin of the spin polarization in this low-concentration range is beyond the well-known intrinsic property of the Hubbard model to stabilize the ferromagnetic state upon an increase of U [33, 34]. To understand the origin of the magnetism, it is instructive to consider the configuration- and spin-projected band occupancies $n_{\alpha\sigma}^j = p_j \sum_{\vec{k}} [1 + \exp(\lambda_{\alpha\sigma}^j(\vec{k}))]^{-1}$. In the magnetic state M_{v1} , the spin polarization m_2 develops due to the nonzero one-vacancy component $m_2^1 = n_{2\uparrow}^1 - n_{2\downarrow}^1 \approx 1$ (Fig. 3(a), right plot). In contrast, the configurations without vacancies and with two and more vacancies near Ti do not contribute to the spin-polarization ($m_2^0 = m_2^2 = m_2^3 = m_2^4 = 0$) which signifies that the one-vacancy-configurations are the dominant contribution to the spin polarization of the e_g -band in the phase M_{v1} .

For M_{v2} neither the cusp point coordinates (n_c, c_c) nor the extent of the magnetic region are affected by a change of the orbital shift Δ_v between $4t_1$ and $6t_1$. Therefore we can expect that the the single-vacancy-contributions do not play a significant role in the development of the state M_{v2} . This feature is confirmed by the analysis of the band factors $n_{\alpha\sigma}^j$, which shows that the nonzero spin polarization in this case appears due to the nonzero two-vacancy-component $m_2^2 = n_{2\uparrow}^2 - n_{2\downarrow}^2 \approx 0.1 - 0.37$ (Fig. 3(b), right plot). The corresponding electron filling n_2 of the e_g -band is much higher than the filling n_1 of the itinerant ($\alpha = 1$)-band (Fig. 3(b)) that also points towards a double-exchange Zener mechanism by which two-band magnetic order develops from the local magnetic moments of clusterized vacancies and is stabilized through the kinetic exchange.

Fig. 4 shows the k -resolved magnon bands calculated from the pole equations of the two-band RPA susceptibility: $\prod_{\alpha} (1 - U\chi_{\alpha}^{+-}(\vec{q}, \omega)) - J_h^2 \prod_{\alpha} \chi_{\alpha}^{+-}(\vec{q}, \omega) = 0$, where the configurationally averaged Lindhard function is $\chi_{\alpha}^{+-}(\vec{q}, \omega) = (1 - c)^4 \sum_j \frac{p_j}{N} \sum_{\vec{k}} \frac{n_{\vec{k}+\vec{q}, \alpha, \uparrow}^j - n_{\vec{k}, \alpha, \downarrow}^j}{\omega + \Delta_{\vec{k}\vec{q}, \alpha}^j}$, and $\Delta_{\vec{k}\vec{q}, \alpha}^j = \lambda_{\alpha, \downarrow}^j(\vec{k}) - \lambda_{\alpha, \uparrow}^j(\vec{k} + \vec{q})$. In both magnetic states M_{v1} (Fig. 4(a)) and M_{v2} (Fig. 4(b)), similar features in the magnon spectrum include the soft Goldstone character of the magnon mode in the Γ point for all defect concentrations. In the M_{v2} state, approaching the critical defect concentration $c_c = 0.12$, which terminates the magnetic states in the phase diagram of Fig. 2, leads also to a magnon softening in the vicinity of the $M(\pi, \pi)$ point. A similar softening near the M point and close to the $X(\pi, 0)$ point is found in the M_{v1} -

state when the critical defect density $c \approx 0.034$ is approached. The magnon softening in M_{v2} state around $M(\pi, \pi)$ is accompanied by a dispersion flattening in the range $c \approx 0.15 - 0.16$. This anomalous behavior reflects the formation of complex nearly dispersionless spin-wave states [35–37]. Fig. 4(c),(e) and Fig. 4(d),(f) show the contours of the imaginary parts (intensities) of the static Lindhard functions $\chi_{\alpha}^{+-}(\vec{q}, 0)$ in the M_{v1} and M_{v2} -states. The itinerant component ($\alpha = 1$) always has a pronounced central peak at the Γ -point (Fig. 4(c)) or close to the Γ -point (Fig. 4(d)) whereas the localized component ($\alpha = 2$) is characterized by high-intensity fragments that develop at nonzero nesting points $(\pm\pi/2, 0)$ and $(0, \pm\pi/2)$ (Fig. 4(e)) and extend to the M -points with increasing c (Fig. 4(f)). The striking difference between the multiband contributions shows that the ferromagnetic order emerges with the spin polarization of the itinerant band, whereas the magnetic polarization of the localized band is controlled by nonzero wavevectors that introduce complex magnetic oscillations [41].

In the phase-separated state of the phase M_{v1} , the key parameter characterizing the stability is the radius of critical magnetic droplets R_c which can be estimated from the minimization of the contributions of the Coulomb energy ε_C and of the droplet surface energy ε_s in both para- and magnetic states. Minimization of $\varepsilon_C + \varepsilon_s$ [38] with respect to R_c results in the expression for the inhomogeneity scale: $R_c = \left(\sigma / u \delta_{fp}^2 \xi^{3/2} [\xi^2 + (1 - \xi)^2] \right)^{1/3}$, where ξ is the magnetic phase content, $u = e^2/16\varepsilon$, the charge imbalance between the para- and magnetic states with the densities n_p and n_f is $\delta_{fp} \sim (n_f - n_p)$, and the surface energy per unit surface is given by $\sigma = t_1 c (1 - c)^3 \left\{ f(m_1, m_2)^2 + \frac{t_1}{t_2} f(m_2, m_1)^2 \right\}$, where $f(x_1, x_2) = (Ux_1 + J_H x_2)/t_1$ and ε is the dielectric constant. The dependence of R_c on the vacancy concentration c is strongly nonlinear, due to the competition between the increase of the surface energy $\sigma \sim c$ for larger values c on account of pinning and the c -driven increase of the vacancy-induced charge-imbalance $\delta_{fp}^2 \sim c^\zeta$ with $\zeta \approx 0.5 - 1$ for $c > c_m$ in the denominator of R_c . In the weak-correlation regime, this leads to a distinct minimum of R_c at $c_m \approx 0.08$, with further linear enhancement of the droplet radius for $c > c_m$ due to the increase of the magnetic surface energy. With $\varepsilon \approx 100$, the characteristic values R_c are in the range of $20a - 100a$. This implies a mesoscopic to microscopic scale of the stable magnetic droplets which is by one to two orders of magnitude larger than the droplet sizes obtained in the scenario of metal-insulator polaron phase separation [27] with polaron-type localization [27, 39], but in agreement with the characteristic scale of inhomogeneities estimated in recent SQUID studies [5].

To conclude, we have revealed unconventional mag-

netic states common for the titanate interfaces which are stabilized above a finite critical concentration of oxygen defects. The magnetic states are characterized by an interplay of ferromagnetic order in the itinerant t_{2g} band and complex magnetic oscillations in the orbitally reconstructed e_g -band, which at oxide interfaces can be tuned by gate fields. The magnetic phase diagram includes highly fragmented regions of stable or phase-separated magnetic states emerging at nonzero critical defect concentrations, mediated by different types of local vacancy configurations.

This work was supported by the DFG (TRR 80). Grants of computer time from the Leibniz-Rechenzentrum München through the SuperMUC project pr58pi are thankfully acknowledged.

-
- [1] A. Ohtomo and H. Hwang, *Nature* **427**, 423 (2004).
 - [2] A. Brinkman *et al.*, *Nature Materials*, **6**, 493 (2007).
 - [3] Lu Li, C. Richter, J. Mannhart, and R.C. Ashoori, *Nature Physics*, **7**, 762 (2011).
 - [4] Ariando *et al.*, *Nature Communications* **2:188**, doi:10.1038/ncomms1192 (2011).
 - [5] J. A. Bert, B. Kalisky, C. Bell, M. Kim, Y. Hikita, H.Y. Hwang, K.A. Moler, *Nature Physics* **7**, 767 (2011).
 - [6] B. Kalisky, J.A. Bert, B.B. Klopfer, C. Bell, H.K. Sato, M. Hosoda, Y. Hikita, H.Y. Hwang, K.A. Moler, *Nature Communications* **3:922**, doi:10.1038/ncomms1931(2012).
 - [7] A. Kalabukhov *et al.*, *Phys. Rev. B* **75**, 121404(R) (2007).
 - [8] G. Berner *et al.*, *Phys. Rev. Lett.* **110**, 247601 (2013).
 - [9] A. Joshua, J.Ruhman, S. Pecker, E. Altman, and S. Ilani, *Proc. Nat. Acad. Sci. USA* **110**, 9633 (2013).
 - [10] J.-S. Lee *et al.*, *Nature Materials*, , (2013).
 - [11] Z.Q. Liu *et al.*, *Physical Review B* **87**, 220405 (R)(2013).
 - [12] M. Salluzzo *et al.*, *Phys. Rev. Lett.* (accepted), arXiv/cond-mat:1305.2226 (2013).
 - [13] W. Han *et al.*, *Nature Communications*, **4:2134** (2013).
 - [14] J. Shen, H. Lee, R. Valenti, and H.O. Jeschke, *Phys. Rev. B* **86**, 195119(2012).
 - [15] W.A. Adeagbo, G. Fischer, and W. Hergert, *Phys. Rev. B* **83**, 195428(2011).
 - [16] I.S. Elfimov *et al.*, *Phys. Rev. Lett.* **98**, 137202 (2007).
 - [17] A.J. Millis, *Nature Phys.* **7**, 749(2013).
 - [18] H. Chen, A.M. Kolpak, and S. Ismail-Beigi, *Adv. Mater.* **22**, 2881(2010).
 - [19] K. Michaeli, A.C. Potter, and P.A. Lee, *Phys. Rev. Lett.* **108**, 117003 (2012).
 - [20] Z. Zhong and P.J. Kelly, *Eur. Phys. Lett.* **84**, 27001 (2008).
 - [21] W.-C. Lee and A.H. MacDonald, *Phys. Rev. B* **76**, 075339 (2007).
 - [22] N. Pavlenko, T. Kopp, E.Y. Tsymbal, G.A. Sawatzky, and J. Mannhart, *Phys. Rev. B* **85**, 020407(R) (2012).
 - [23] N. Pavlenko, T. Kopp, E.Y. Tsymbal, J. Mannhart, and G.A. Sawatzky, *Phys. Rev. B* **86**, 064431 (2012).
 - [24] N. Pavlenko and T. Kopp, *Surf. Sci.* **605**, 1114 (2011).
 - [25] R. Pentcheva and W.E. Pickett, *Phys. Rev. B* **74**, 035112 (2006).
 - [26] K. Janicka, J.P. Velev, and E.Y. Tsymbal, *J. Appl. Phys.* **103**, 07B508 (2008).
 - [27] B.R. Nanda and S. Satpathy, *Phys. Rev. B* **83**, 195114 (2011).
 - [28] P. Fazekas, *Lecture Notes on Electron Correlation and Magnetism* (World Scientific, Singapore, 1999).
 - [29] M. Breitschaft *et al.*, *Phys. Rev. B* **81** 153414 (2010).
 - [30] N. Pavlenko and T. Kopp, *Phys. Rev. B* **72**, 174516 (2005).
 - [31] N. Pavlenko and F. Schwabl, *Appl. Phys. Lett.* **86**, 012507 (2005); N. Pavlenko and F. Schwabl, *Applied Physics A: Materials Science & Processing* **80**, 217 (2005).
 - [32] R.J. Elliot, J.A. Krumhansl, and P.L. Leath, *Rev. Mod. Phys.* **46**, 465 (1974).
 - [33] J.E. Hirsch, *Physical Review B* **31**, 4403 (1985).
 - [34] N. Pavlenko and T. Kopp, *J. Supercond. Nov. Magn.* **26**, 1175 (2013).
 - [35] P. Moch, G. Parisot, R.E. Dietz, and H.J. Guggenheim, *Phys. Rev. Lett.* **21**, 1596 (1968).
 - [36] S.K. Lyo, *Phys. Rev. Lett.* **28**, 1192 (1972).
 - [37] R. Alben, S. Kirkpatrick, and D. Beeman, *Phys. Rev. B* **15**, 346 (1977).
 - [38] J. Lorenzana, C. Castellani, and C. Di Castro, *Physical Review B* **64**, 235127 (2001).
 - [39] N. Pavlenko and T. Kopp, *Phys. Rev. Lett.* **97**, 187001 (2006).
 - [40] For a 100 Å-thick gate layer, the typical values of the gate potential $V_g \sim 10^6$ V/cm induce maximal electron energy shifts E_g of about 1.0 eV.
 - [41] Magnetic oscillations in coordinate space will appear due to the coupling/scattering of spin density waves generated by localized defects or defect clusters in an itinerant ferromagnetic background.